

University of  
St Andrews

# SIMULATING LASER DOPPLER FLOWMETRY USING MONTE CARLO METHODS

**Mphys Project Review**

By: Callum Gouveia Da Silva

ID: 110006452

Project Supervisor: Kenneth Wood

Final Word Count: 7623

## CLARIFICATION OF ORIGINAL CONTENT

Of the work presented within this report all graphs, illustrations, data, code and conclusions have been my own unless otherwise stated, with the following exceptions:

- The 3-Dimensional grid code on which the simulation was built and the methods described in the “Depth of Propagation” section are based on work by Dr Kenneth Wood. I have made some modifications to this particular part of the code by upgrading it from FORTRAN 70 to FORTRAN 90, and by inserting my own system for tracking photons. All of the density structures within the grid are also my own design.
- The 3-Dimensional scattering angle calculations described in the “Direction of Propagation” section were performed by code originally written by Dr Kenneth Wood. I have upgraded this section of code from FORTRAN 70 to FORTRAN 90.

## CONTENTS

Abstract .....	4
Introduction .....	4
Laser Doppler Flowmetry .....	4
The LAKK-M MLNDS Device .....	5
The Tissue Model .....	5
Absorption Coefficients .....	6
Scattering Coefficients .....	7
Blood Vessels .....	8
Photon Propagation .....	11
Depth of Propagation .....	11
Direction of Propagation .....	12
Frequency Shift .....	14
Photon Tracking .....	14
Detection .....	15
Results and Analysis .....	17
Fluence Rates .....	17
Doppler Shifts .....	19
The Detected Signal .....	20
Further Development .....	24
Conclusions .....	25
Bibliography .....	26

## ABSTRACT

Microvascular dysfunction in the skin is a marker for a number of cardiovascular diseases. Assessing the flow rate and reactivity of the skin microcirculation could therefore present a unique avenue for diagnosis. Laser Doppler Flowmetry (LDF) is one such technique that allows for the non-invasive measurement of perfusion in the blood. When applied to the skin surface, laser light acquires a Doppler shift from moving red blood cells in the papillary dermis. This Doppler signal is proportional to the flux of red blood cells through the illuminated tissue. Although the technology is promising, readings can vary substantially between different patients and skin sites.

In order to gain further insight into the Doppler signal, a computer simulation of the process was constructed using the Monte Carlo technique. The simulation produces a randomly generated web of arterioles and capillaries within layers of epidermal and dermal tissue. Photons are then applied to the model and any shifts in frequency are measured. The simulated Doppler signal can finally be traced back to the exact capillaries and arterioles that produced it and the effects of varying vessel density can be observed and quantified. Using these methods a relationship was found between the sensitivity of the perfusion measurement and simulated vessel density that may aid in the standardisation of clinical measurements.

## INTRODUCTION

In 1947, Stanislaw Ulam considered the card game Solitaire and how he might calculate the probability of winning. After some thought, he realised that by playing enough games he could sample the underlying probability distribution enough times to gain a good estimate. From this principle, the Monte Carlo technique was born. [1] Monte Carlo codes allow the solutions to very complex problems to be estimated without the problem itself being analytically solved. If a laser is applied to section of biological tissue for example, the corresponding wave equations can become impossibly complex when the various heterogeneities are taken into account. If we instead consider the beam to be comprised entirely of photons in a statistical mixture, we can calculate the path of an individual 'sample' photon. Our sample photon can be propagated along a random optical depth before it is either absorbed or scattered and propagated further. If we know the probabilities of scattering and absorption, and these values are accurate, then when enough photons have been propagated the sum of their fluences will recreate the profile of the original beam. This is all achieved without solving any wave equations. [1]

In this Project Review, the Monte Carlo technique has been used to simulate a particular form of clinical laser diagnosis called 'Laser Doppler Flowmetry' (LDF).

## LASER DOPPLER FLOWMETRY

The Doppler Effect is a well-known optical phenomenon. When light encounters a moving scatterer or is emitted by a moving source, its frequency is shifted accordingly. This is most commonly described by the equation:

$$\Delta f = \frac{\Delta v}{c} f_0$$

(Eqn. 1)

Thus, the magnitude of the Doppler shift scales with the velocity of the scatterer. When a laser beam is applied to the surface of human skin, photons are scattered by moving red blood cells in the microcirculation just below the epidermis. This induces a Doppler shift that scales with the product of red blood cell concentration and velocity yielding a single value known as 'perfusion'. [2]

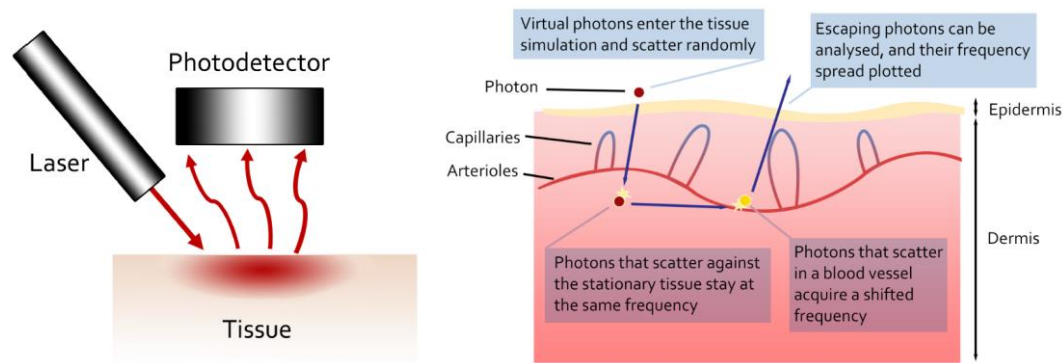


(Fig. 1) These illustrations show the general principles behind the LDF technique and how it can be simulated. Abstractions have been made when modelling the structure of the skin and blood vessels. [3]

By measuring the frequency broadening of laser light returning to the skin's surface, it is possible to measure this perfusion value non-invasively. This is medically very significant because poor blood flow or responsiveness in the microcirculation, known as microvascular dysfunction, is a marker for diabetes and a variety of cardiovascular diseases. In its current state, LDF can provide only relative perfusion values in arbitrary units. While this can be useful in assessing the response of a subject's microcirculation to stimuli, results from different patients cannot be easily compared. It is hoped that with a better understanding of the variation in LDF signal between patients and skin sites, a method to reliably measure perfusion and possibly diagnose problems could be discovered. [4] We are therefore motivated to learn more about this LDF signal and how it is affected by heterogeneities in the skin. A Monte Carlo simulation of the skin is one way in which this can be explored.

#### THE LAKK-M MLNDS DEVICE

The simulation was designed to help in the interpretation of clinical measurements made by collaborators at Ninewells Hospital and Medical School in Dundee. These physical measurements were made using a device called the LAKK-M multifunctional laser non-invasive diagnostic system (MLNDS). If results from the model are to be compared with real values, the simulated measurement process must follow the physical process as closely as possible. The device features an array of lasers within a single probe and is capable of collecting data on a variety of tissue features including perfusion, tissue oxygen saturation and relative blood volume. [5] The simulation used the following parameters to mimic the LAKK-M's LDF probe in particular:

Source Wavelength	1064nm
Beam Radius	0.4mm
Detector Radius	0.4mm
Probe-Detector Center Separation	1mm

#### THE TISSUE MODEL

A tissue model was created for Monte Carlo photons to interact with. The full structure of the skin is highly complex and contains a vast array of components including hair follicles, collagen fibres, various blood vessels and sweat glands. [6] These are only a small number of the important components making it unfeasible to simulate everything. In LDF we are primarily concerned with the distribution of blood vessels as these are responsible for the detected signal. Abstractions of the other skin components could therefore be made. The final tissue model consisted of two primary layers: An epidermis characterised by strong absorption from melanin (a skin pigment), and a generic dermis material in which discrete blood vessels were generated. As shall be explained later, these blood vessels were created randomly to reproduce the heterogeneities seen in natural

skin. The microcirculation of real skin begins at very small blood vessels downstream from the arteries known as arterioles. These are paired with similarly small vessels containing deoxygenated blood known as venules. Small  $\sim 5\mu\text{m}$  capillaries connect the two and deliver blood to the tissues. [3][7] To accelerate the generation of these blood vessels and maintain the general structure, further abstractions had to be made. The modelled blood vessels consist entirely of arterioles moving across the simulation area. Capillary loops are distributed along these arterioles as illustrated in *fig.1*.

The model consists of a rectangular grid of cubes referred to as 'cells'. Each cell has its own density, absorption, blood velocity, net photon fluence and average photon wavelength. Every cell has the same size which is determined by the simulation settings.

Upon initialisation, this grid and all cells within are populated in two waves:

- 1) The macrostructure generation
- 2) The microstructure generation

In the first wave, the grid is separated into the two distinct layers described earlier: the epidermis and the dermis. The epidermal layer lies on the skin surface acting as a simple absorber. The second layer is the dermis in which the capillaries and arterioles reside. Every cell in the upper  $73\mu\text{m}$  is considered to be in the epidermis, and any cell below is part of the dermis. This depth was chosen to emulate the forearm of a young person approximately 23 years of age. [8] Each cell is then assigned optical properties corresponding to its given layer.

## ABSORPTION COEFFICIENTS

Most conventional optical properties of the dermis describe the general behaviour of light propagating through it. The value represents the average scattering or absorption across all collagen fibres, internal pigments, blood vessels and other structures. Previous works on modelling the LDF process have used a similarly generic dermis. In these cases when a photon is scattered any frequency change is determined by its statistical chance of striking a blood vessel based on density. [9] [10] While this approach can reliably reproduce the LDF frequency spectrum, it offers less insight into the effects of heterogeneities within the skin. It is for this reason that the tissue simulation described here features discretely generated blood vessels. If the blood vessels are to be separated from the generic dermis, their optical properties must also be extracted. A work by Steven Jacques describes how absorption spectra in various tissues can be constructed by the separate absorbers (or 'chromophores') within. Absorption within the dermis can be broken down into a few key components that include water, oxy/deoxy haemoglobin, fat and pigments. [11] Using this method, we can generate the following absorption parameters for the dermis and blood:

$S$	HGb oxygen saturation of mixed arterio-venous vasculature
$B$	average blood volume fraction ( $f_{v,\text{blood}}$ )
$W$	water content ( $f_{v,\text{water}}$ )
$Bili$	bilirubin concentration ( $C$ (M))
$\beta C$	$\beta$ -carotene concentration ( $C$ (M))
$F$	fat content ( $f_{v,\text{fat}}$ )
$M$	melanosome volume fraction ( $f_{v,\text{melanosome}}$ ), or alternatively the molar concentration of melanin monomers ( $C$ (M)).

The total absorption coefficient is calculated

$$\mu_a = BS\mu_{a,\text{oxy}} + B(1 - S)\mu_{a,\text{deoxy}} + W\mu_{a,\text{water}} + F\mu_{a,\text{fat}} + M\mu_{a,\text{melanosome}} + 2.3C_{\text{bili}}\epsilon_{\text{bili}} + 2.3C_{\beta C}\epsilon_{\beta C}.$$

(Eqn. 2) Absorption coefficient for a generic tissue, S. Jacques [11].

In the near-IR at which our laser is operating, the total absorption by bilirubin and  $\beta$ -carotene can be assumed negligible. [11]  $\mu_{a,oxy}$  and  $\mu_{a,deoxy}$  refer to the absorption of oxygenated and deoxygenated haemoglobin respectively.

Layer	S	B	W	F	M	Total $\mu_a$
Epidermis	0%	0%	0%	0%	2.5%	$\mu_a = 0.025 \times \mu_{a,melanosome} = 0.379 \text{ mm}^{-1}$
Dermis	39%	$0.2\% \times d$	65%	0%	0%	$\begin{aligned} \mu_a &= 0.02 \times 0.39 \times \mu_{a,oxy} \\ &\quad + 0.02 \times (1 - 0.39) \\ &\quad \times \mu_{a,deoxy} \\ &\quad + 0.65 \times \mu_{a,water} \\ &= 9.34 \times 10^{-2} \text{ mm}^{-1} \end{aligned}$

Coefficient	Value at 1064nm	Source
$\mu_{a,melanosome}$	$15.16 \text{ mm}^{-1}$	$\mu_{a,melanosome} = (519 \text{ cm}^{-1}) \left( \frac{\lambda}{500 \text{ nm}} \right)^{-m}; m = 3$ [12]
$\mu_{a,oxy}$	$1.07 \text{ mm}^{-1}$	UCL [13]
$\mu_{a,deoxy}$	$0.138 \text{ mm}^{-1}$	UCL [13]
$\mu_{a,water}$	$1.44 \times 10^{-2} \text{ mm}^{-1}$	Kou et al. [14]

The dermal blood factor, ' $d$ ' describes the proportion of blood remaining within the dermis. A factor of 0 removes all haemoglobin absorption, whereas a factor 1 of is a generic dermis containing blood vessels. The amount of diffuse blood outside of the dermal vessels is not well determined and so by including this as a variable the two extremes can be explored.

The  $\mu$  coefficients used were based on absorption spectra from a variety of sources. Haemoglobin and water absorption does not behave in an easily modelled way across different wavelengths. Spectra from different sources therefore had to be imported and interpolation used to find a value corresponding to the laser wavelength. Reliable data for blood absorption in the 1064nm regime is difficult to find in literature [15], and so linear extrapolation had to be used from the 1050nm UCL data based on the general behaviour observed by Troy et al. [16]

## SCATTERING COEFFICIENTS

A more difficult parameter to determine is the scattering coefficient of the dermis. Again, Jacques presents a general formula for the scattering properties of various tissues (Eq.3). The ' $g$ ' factor seen here describes the isotropy of the scattering. It has a universal value of 0.95 and is part of the Henrey-Greenstein phase function that shall be explained later. The other ' $a$ ' and ' $b$ ' parameters are empirical and tissue specific. Whole blood is included in the list of these parameters; the equation can be used for the arterioles and capillaries in the simulation. [17] No such value exists for a bloodless dermis however. As Jacques explains, the scattering behaviour in a tissue can be broken down into two types: Rayleigh scattering and Mie scattering. Rayleigh scattering dominates at long wavelengths such as IR and near-IR whereas Mie scattering dominates in the shorter visible range. The tissue simulation will be emulating a laser in the 1064nm regime, meaning Mie scattering will be negligible. [17] Further investigation into Rayleigh scattering reveals that it originates from large structures in the dermis such as collagen fibres. This means that we can assume the blood contribution will be small and use an unmodified dermal scattering coefficient provided that we only operate in the near-IR or beyond. [18]

$$\mu'_s = a \left( \frac{\lambda}{500 \text{ (nm)}} \right)^{-b} ; \mu_s = \mu'_s \times (1 - g)$$

(Eqn.3) Scattering coefficient for a generic tissue, S. Jacques [17]

Coefficient	Value at 1064nm	Source
$\mu_{s,epidermis}$	$a = 68.7 \text{ cm}^{-1}$ ; $b = 1.161$ ; $\mu_{s,epidermis} = 57.18 \text{ mm}^{-1}$	[17]
$\mu_{s,dermis}$	$a = 45.3 \text{ cm}^{-1}$ ; $b = 1.292$ ; $\mu_{s,dermis} = 34.15 \text{ mm}^{-1}$	[17]
$\mu_{s,blood}$	$a = 22 \text{ cm}^{-1}$ ; $b = 0.66$ ; $\mu_{s,blood} = 26.73 \text{ mm}^{-1}$	[17]

With these values in place, the epidermis and bloodless dermis can be generated with their corresponding optical properties. The dermis can then be populated with blood vessels in the microstructure phase.

### BLOOD VESSELS

In order to emulate the heterogeneities seen in live tissue, the blood vessels are generated using a variant of the random walk technique. A starting point is chosen randomly at any edge of the sample and a vessel direction vector is assigned along the normal to this edge. A small  $1 \mu\text{m}$  cylinder is created with its long axis parallel to this vector and any grid cells within are given the optical properties of blood. The end of this cylinder is then used as a starting point for the next generation which begins pointing towards a new randomly shifted direction as shown in Fig.2. The process then repeats and the blood vessel begins to ‘snake’ across the tissue until it reaches any edge of the grid where it is then terminated. The magnitude of this walk in the horizontal and vertical directions can be adjusted separately, allowing the shapes of the vessels to be tweaked according to physical measurements.

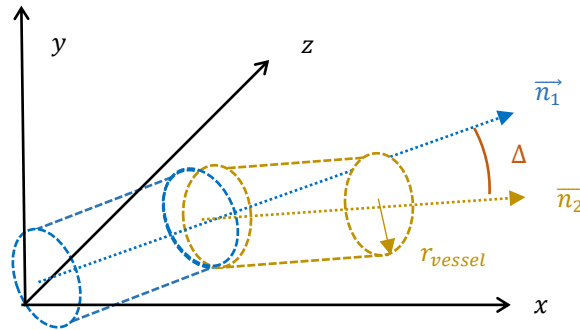


(Fig. 2) The blood vessels are created by chaining together strings of small cylinders. Each successive cylinder vector  $n$  is a small angular deviation  $\Delta$  from the previous  $n$ .



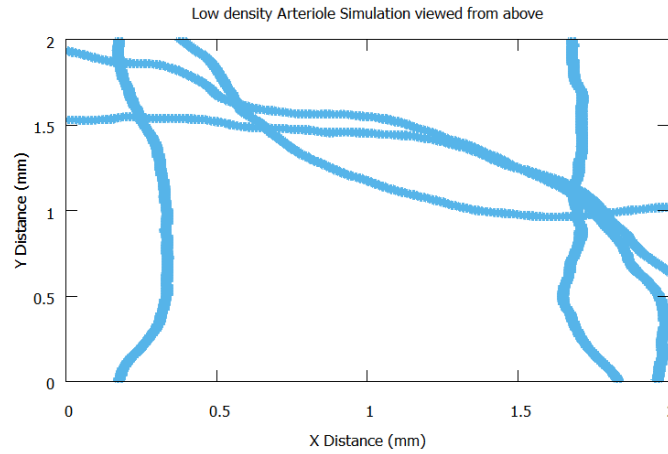
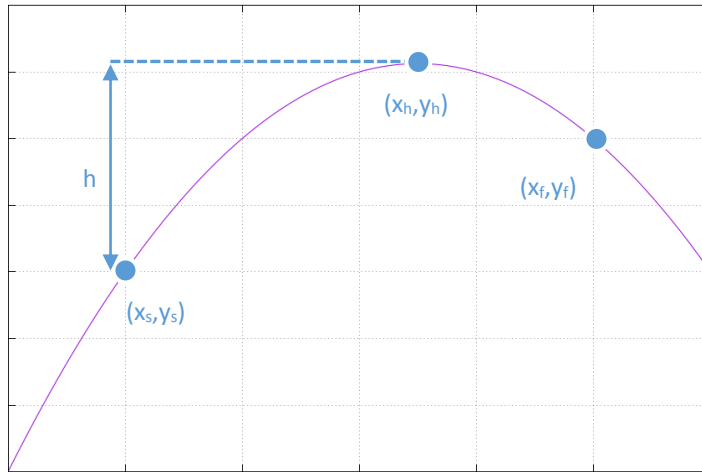


(Fig.3) An example of a low-density arteriole network produced by the simulation

While this generation is taking place capillary sites are interspersed evenly along the arteriole. Once all arterioles are complete the capillary generation begins. The program will iterate through these sites pairing the closest together. Using a semi-randomly determined height, a parabola can be generated between our two points using the parametric solution shown in Eqns. 4. There are two possible curves; we select the solution in which the vertex lies between both the start and end points.



At any point on the parabola:

$$|x - x_h| \propto \sqrt{|y - y_h|}$$

Using this ratio we can introduce the parameter  $t$ :

$$t = \frac{\sqrt{|y_s - y_h|}}{\sqrt{|y_s - y_h|} + \sqrt{|y_f - y_h|}}$$

This  $t$  represents the relative distance the vertex lies between our start and end points. Hence,  $x_h$  can be found:

$$x_h = (1 - t)x_s + t x_f$$

Allowing the curve to be easily solved.

(Eqns. 4)

(Fig.4) A parabolic capillary shape can be determined using a start co-ordinate, end co-ordinate and a desired height.

A small cylinder is made to follow this parabola and is used to fill in the optical properties of the blood in the same way as the arteriole generation. The end result is a network of arterioles with parabolic capillaries attached as seen in Fig.5.

Low density Arteriole Simulation in 3 dimensions

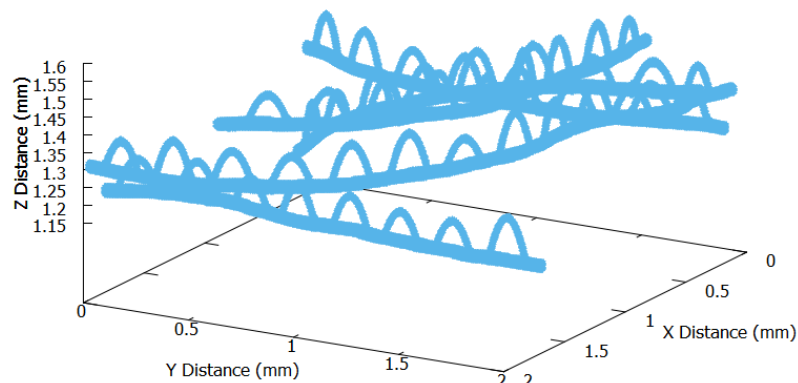


(Fig.5) A 3-dimensional example of a low density blood vessel simulation. Arterioles form the horizontal branches with the capillaries looping along the z-direction.

Although randomly generated, this tissue structure needs to approximate a real section of skin to be of clinical use. The system described above was therefore used as a toolset to emulate the following skin biopsies by Bravermann et al. [19]:

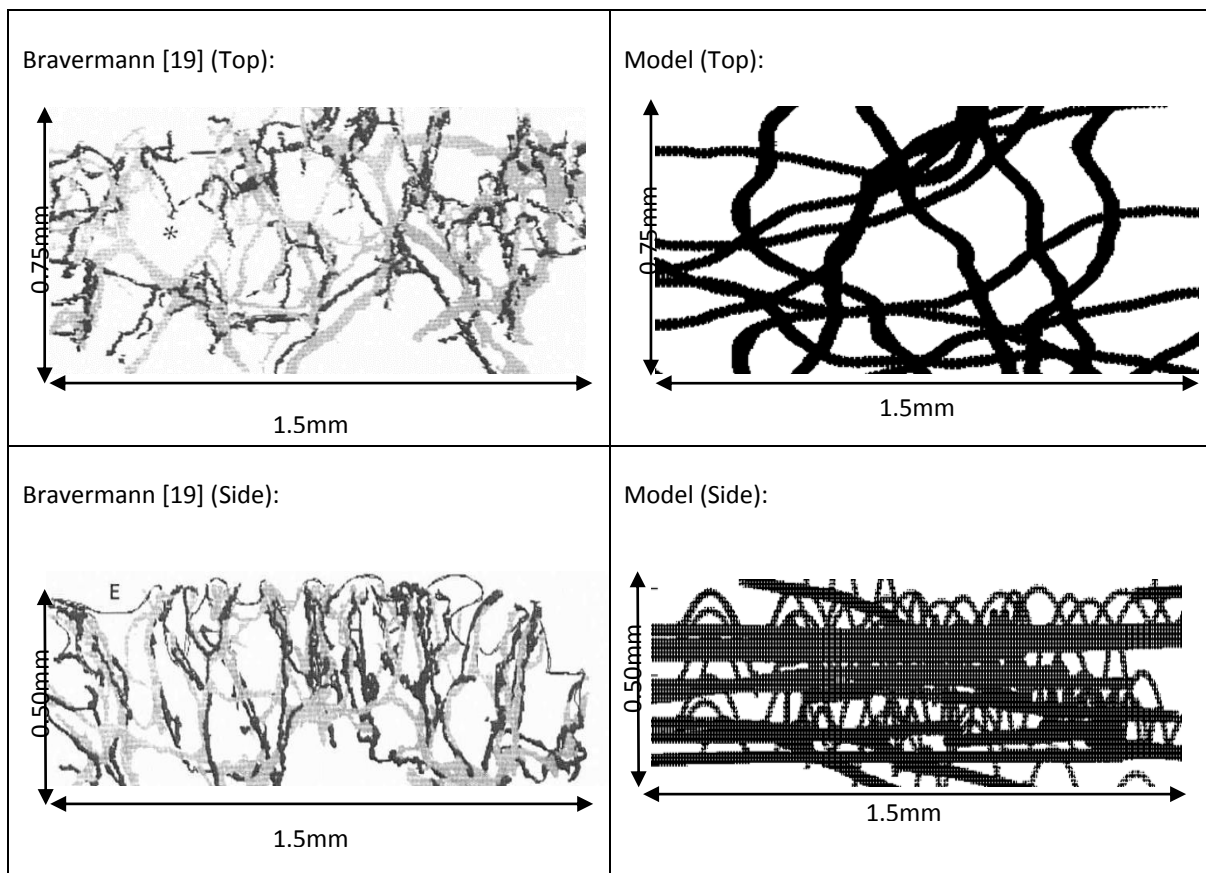


(Fig. 6) – Comparisons between tissue biopses and generated tissue model.

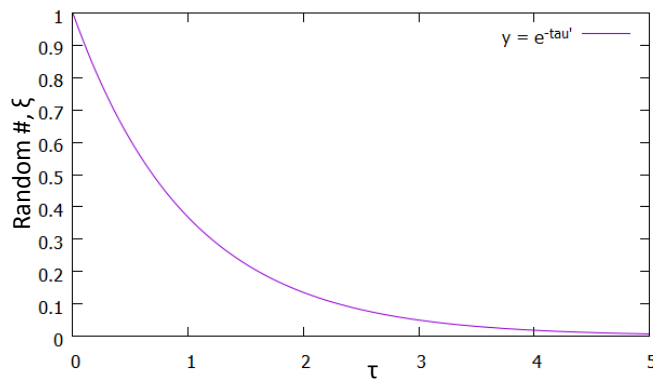
In the Bravermann images the dark lines represent arterioles and lighter lines venules. The vessel walls in the Bravermann images are not pictured and therefore appear thinner than the model equivalents. Venules and arterioles in the model are also considered identical. The random walk magnitude was increased until the bloodless ‘empty’ regions were of similar size and frequency when viewed from above. The arteriole depth range was then estimated from the side biopsy. Only the upper ~0.5mm was considered, as this was the penetration depth of the laser. There is a clear discrepancy between the biopsy and model when viewed from the side. This is because the Bravermann paper was primarily concerned with ‘ascending elastic arterioles’. The skin site was chosen for a biopsy because arterioles were rising to the surface from below [19]. In the model however, the arterioles are always generated from the edge of the tissue and primarily move horizontally. Although the vertical walk can be enhanced this led the arterioles to unrealistically drift out of the top or bottom of the grid before they could reach the other side. The arterioles were therefore configured to remain largely within the vertical plane in which they were generated. This approach instead followed more general depictions of the upper papillary dermis [3].

## PHOTON PROPAGATION

With a tissue of discrete structures and corresponding optical properties in place, the model then needed to facilitate the propagation of photons in a realistic manner.

### DEPTH OF PROPAGATION

As explained earlier, the tissue consists of cubic cells in a grid. Photons enter the grid in turn from a random point within a circular source region just above the tissue, which emulates a laser beam. A random optical depth is then chosen for each photon as shown in Fig.7



$$\xi = \int_0^{\tau} e^{-\tau'} d\tau' = 1 - e^{-\tau}$$

$$\Rightarrow \tau = -\log(1 - \xi)$$

As  $\xi$  is a random number between 0 and 1:

$$\tau = -\log(\xi)$$

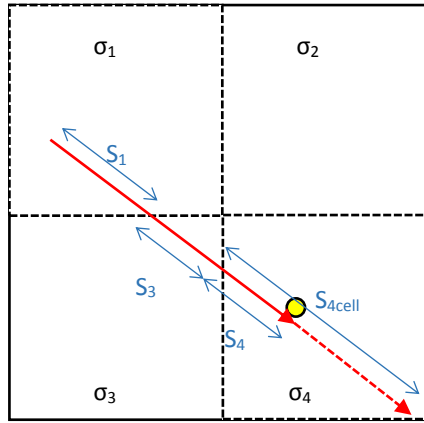
This tau is an optical depth, and thus by definition it can be used to obtain a random distance L via:

$$\tau = \int_0^L n\sigma ds$$

(Eqns. 5) [20]

(Fig.7) The photon's penetration probability decreases exponentially with depth. This depth can be obtained by integrating through an exponentially decaying probability density function as shown.

As shown above, the actual distance associated with an optical depth is determined by an integral of the density and cross section of a tissue being traversed. By convention, the optical depth ‘ $n$ ’ and cross section ‘ $\sigma$ ’ are combined into a single coefficient, ‘ $\sigma$ ’ that represents the scattering and absorption cross sections in a particular material. This ‘ $\sigma$ ’ will vary depending on whether a region of dermis, epidermis or blood vessel is being crossed. As the tissue is broken into discrete cells, we can replace the integral with a summation and numerically iterate along the photon's path. [20]



For each cell along a photon's path, we update running values of  $\tau$  and the corresponding distance  $s$ .  $\tau_{run}$  represents the current optical depth traversed by the photon, and  $S_{total}$  the physical distance. Eventually, the running  $\tau$  will exceed our randomly generated  $\tau_{photon}$ . This can be seen in the adjacent example:

$$\tau_{run} = S_1\sigma_1 + S_3\sigma_3 + S_{4cell}\sigma_4 > \tau_{photon}$$

When this condition is met our photon cannot traverse the entire final cell. We simply take the difference in  $\tau$  values:

$$\tau_4 = \tau_{run} - \tau_{photon}$$

and use this final result to complete our distance:

$$S_4 = \tau_4 / \sigma_4$$

$$S_{total} = S_1 + S_3 + S_4$$

(Eqns.6) [20]

(Fig. 8) A photon travels along a random path indicated by the solid red line. It passes through 3 different cells along the way. The total distance required to pass through cell 4 (dotted line) is longer than the given random depth. After some calculation a point of interaction is determined (shown in yellow).

At the end of the randomly chosen optical depth, an interaction takes place between the photon and the tissue. There are two types of interaction considered by the simulation: absorption and scattering. The probability of each process is simply determined by the relative size of the absorption and scattering coefficients within the interaction cell. This probability is contained in a parameter known as the 'albedo':

$$a = \frac{\sigma_s}{\sigma_a + \sigma_s}$$

(Eqn. 7) [20]

If a randomly generated number between 0 and 1 is less than this albedo, then the photon has been absorbed and is removed from the simulation immediately. Otherwise, the photon has scattered. A new direction of propagation is determined and a new optical depth obtained randomly. The simulation then continues propagating the photon until it is eventually absorbed or it leaves the bounds of the grid. [20]

## DIRECTION OF PROPAGATION

Each random direction of photon propagation is determined by the Henyey-Greenstein (H-G) phase function. This phase function yields a direction weighted towards the photon's propagation vector and can produce a light distribution closer to that observed in reality. [21] The H-G function contains a parameter 'g' that determines the magnitude of this forward weighting. In the tissue simulation, a universal value of 0.95 was used based on skin measurements in the 1000nm regime. [17].

The H-G function used in the simulation has the following form [22]:

$$p(\mu) = \frac{1}{2} \frac{1 - g^2}{[1 + g^2 - 2g\mu]^{3/2}}$$

(Eqn. 8)

Where  $\mu = \cos(\theta_{scattering})$ , and  $\theta_{scattering}$  is the angle of scattering relative to the direction of photon propagation. This yields a probability distribution over  $\mu$  from which the random angle can be obtained.

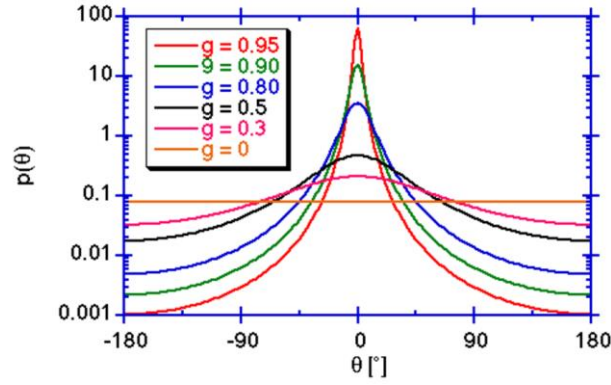


Image: Oregon Medical Laser Center [23]

(Fig 9) An example of the scattering probability distribution induced by the H-G function.

In order for this equation to be applied, the angle of scattering has to be converted from the photon frame to the lab frame (relative to the static co-ordinate system of the tissue). This is achieved using the following relationship: [24]

$$n_x^{new} = \frac{\sin\theta_s (n_x n_z \cos\varphi_s - n_y \sin\varphi_s)}{\sqrt{1 - n_z^2}} + n_x \cos\theta_s$$

$$n_y^{new} = \frac{\sin\theta_s (n_y n_z \cos\varphi_s - n_x \sin\varphi_s)}{\sqrt{1 - n_z^2}} + n_y \cos\theta_s$$

$$n_z^{new} = -\sin\theta_s \cos\varphi_s \sqrt{1 - n_z^2} + n_z \cos\theta_s$$

(Eqns. 9)

Where  $\mathbf{n} = (n_x, n_y, n_z)$  is the initial photon direction, and  $\mathbf{n}_s = (n_x^{new}, n_y^{new}, n_z^{new})$  is the scattered photon direction shifted to the lab frame based the H-G angle of scattering,  $\theta_s$  and an isotropic radial direction  $\varphi_s$ .

## FREQUENCY SHIFT

When a photon is scattered within a cell its frequency is shifted according to the cell's blood velocity. For most of the tissue this velocity is 0 and the frequency is unaffected. Within a blood vessel however, there is a velocity vector pointing in the direction of blood propagation. In this case, a Doppler shift is applied using the following formula presented by Fredriksson et al. [25]:

$$\Delta f = -\mathbf{v} \cdot \mathbf{q} = -\mathbf{v} \cdot (\mathbf{k}_i - \mathbf{k}_s)$$

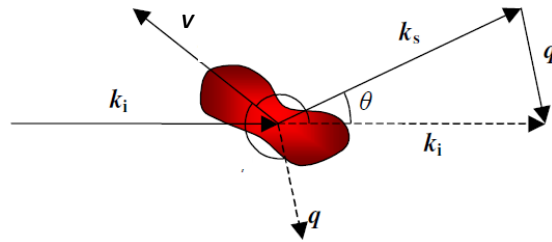


Image: Fredriksson et al. [25]

(Fig.10) An incoming photon along the vector  $\mathbf{k}_i$  is scattered by a blood vessel travelling along  $\mathbf{v}$ . The change in  $\mathbf{k}$  (denoted as  $\mathbf{q}$ ) determines the size and direction of the induced frequency shift.

The dot product takes the projection of  $\mathbf{v}$  along  $\mathbf{q}$ . Hence the classic Doppler formula shown earlier is just a special case where motion is along the line of sight. This frequency shift is remembered by the photon and will accumulate with each subsequent frequency shift until the photon is terminated or detected.

## PHOTON TRACKING

The movement of photons through the model is only useful if they are tracked and processed sufficiently. The simulation collects the following information as photons are propagated:

- Photon fluence rate per cell
- Average photon frequency per cell
- Entire photon path if 'detected'

## PHOTON FLUENCE RATE

Photon fluence rate is used to describe the relative flux of photons through the model. It is calculated using the following formula [26]:

$$J_i = \frac{L}{N\Delta V_i} \sum l_i$$

Where  $J_i$  is the fluence rate of a particular cell,  $\Delta V_i$  is the volume of cell  $i$  and  $\sum l_i$  describes the sum of all photon path lengths within cell  $i$ .

## PHOTON FREQUENCY

Each cell contains an internal sum of all the photon path lengths travelled through it, and a separate sum of the path-weighted frequency shifts it has encountered. At the end of the simulation execution, each cell divides its frequency sum by its path sum to yield an average photon frequency shift as an absolute value:

$$\langle \Delta f_i \rangle = \frac{\sum |f_j - f_{laser}| \times l_j}{\sum l_i}$$

Where  $f_j$  is the frequency of photon  $j$  as it travels through the cell. This allows Doppler maps of the tissue to be produced, highlighting regions in which frequency shifts have taken place.

## PHOTON PATHS

The aforementioned fluence and Doppler maps describe photon behaviour in the tissue as a whole, but only a portion of the incident light contributes to the detected signal in clinical tests. As the path of each photon is randomly determined, it is only possible to tell if a particular photon contributes to the signal once it has completed its trajectory. For this reason, every photon has its complete path recorded while it is being simulated. Upon completion, if the photon has not entered a designated 'detector' area its path information is discarded. Otherwise, the photon path is stored for processing later. Once the simulation is completed and grid information has been written to file, fluence and Doppler information in the grid can be cleared. The stored photon paths are now 'played back' through the simulation, creating a new set of Doppler and fluence maps containing the detected signal exclusively.

## DETECTION

When photons enter the detector region their frequencies are counted in 'bins' of equal width. Each bin is associated with a particular frequency range and contains a tally that increases by 1 with each photon. By allowing many photons to hit the detector, we can obtain a discrete distribution that emulates the optical Doppler spectrum observed clinically. [27]

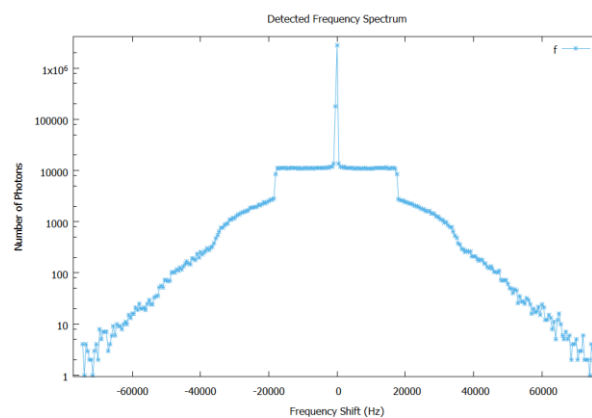


(Fig.11) An example of the measured 'optical Doppler spectrum'. Frequencies are counted into columns of equal width. Interpolation is then used between adjacent columns to produce a line graph.

The Doppler shifts shown in Fig.11 are evenly distributed about the origin because photons have scattered multiple times before reaching the blood vessels. Their directions have been randomised, and so the direction of Doppler shifting is also random [25]. There is an unusual shape near the origin. This 'top-hat' is the single Doppler-scattering region. Photons in this region have been Doppler shifted only once before being detected.

This feature is the result of an idealised blood velocity map in which all arteriole blood has exactly the same speed. In reality there will be a larger spread of velocities and greater signal noise which causes a smoothing of this scattering peak.

This frequency spectrum still needs to be converted into a single perfusion value in order to draw comparisons with clinical measurements. Some processing is first needed to achieve this. It has been shown that the autocorrelation of the optical Doppler spectrum seen above can approximate the power spectral density (PSD) of the photodetector [25]:

$$P(\omega) \propto I(\omega) \star I(\omega)$$

Where  $I(\omega)$  is the optical Doppler spectrum seen in Fig.11, and  $\star$  denotes the autocorrelation. This autocorrelation can be performed by mixing each binned value with every other binned value:

$$P(\omega_i) = \sum_{j=1}^{N_{bins}-i} I(\omega_i) \times I(\omega_{i+j}) ; i \neq j$$

Using this equation, we can generate the PSD shown in Fig.12. This figure represents the frequency content that we might expect in a physical detector current caused by the interference of Doppler-shifted light on the sensor surface [25]. We also see that the single-scattering artefact has persisted through the PSD transformation. This is not necessarily a concern because our desired perfusion value is arbitrarily scaled. As long as it scales linearly with blood velocity, we can draw comparisons with physical measurements.

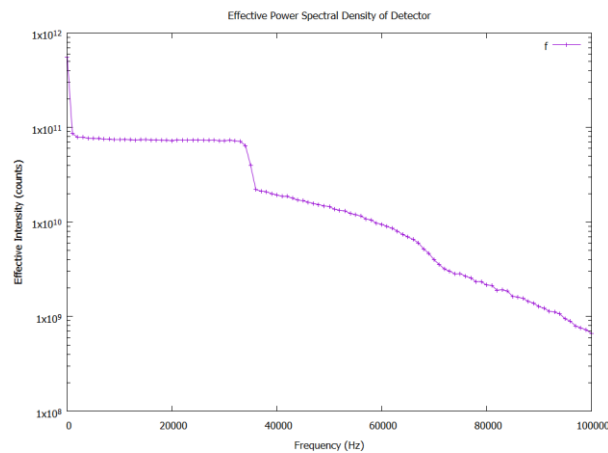


(Fig.12) The virtual detector's PSD computed from the optical Doppler spectrum. This is an 'effective PSD' designed to mimic the current found in a physical photodetector signal.

As shown by Fredriksson et al. [25], by numerically integrating this PSD we can finally obtain values for both perfusion *and* the concentration of moving blood cells (CMBC):

$$Perf \propto \int_0^{\infty} \omega P(\omega) d\omega$$

$$CMBC \propto \int_0^{\infty} P(\omega) d\omega$$

As shall be shown in our results, this perfusion does in fact scale linearly with blood velocity in a way comparable to clinical measurements, and CMBC similarly scales with the density of our blood vessels.



## RESULTS AND ANALYSIS

Once complete, the simulation exports all internal information into a selection of .dat files. These files contain data arranged into two-dimensional tables. The exported information includes:

- Fluence and wavelength information for every cell on the grid (corresponding to all photons and detected photons separately)
- The detected optical Doppler spectrum
- The optical density of the grid
- A log of calculated perfusion and CMBC values and their corresponding photon, blood flow and blood vessel settings

The majority of saved information relates to the 3D simulation grid, and this data cannot be described in its entirety in two dimensions. Therefore, slices of the grid are taken and presented for a particular depth.

### FLUENCE RATES

Photon fluence rates within grid are shown below at varying depths.

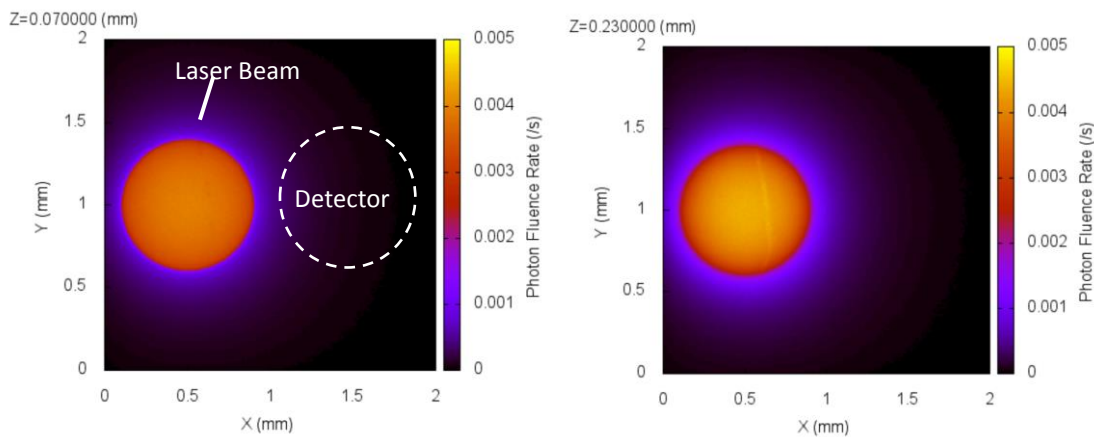


(Fig.13) Fluence maps of the tissue simulation viewed from above near the tissue surface.

In Fig.13 the input laser beam and detector are separated by 1mm in accordance with the LAKK-M design. The laser beam can be easily seen, and is directed towards the +Z direction into the page. The majority of the laser light is constrained in a cylinder directly below the path of the laser beam. Capillaries can be seen in the highest layer as faint elliptical dots. They branch upwards from the arterioles in the negative Z direction out of the page.

At 0.23mm depth, a surface arteriole in the path of the beam becomes bright. At this depth, the higher scattering coefficient in the blood is causing a greater number of scattering events. The blood is experiencing a greater photon fluence than the more transparent dermis because scattered photons have the opportunity to travel through a particular cell multiple times.

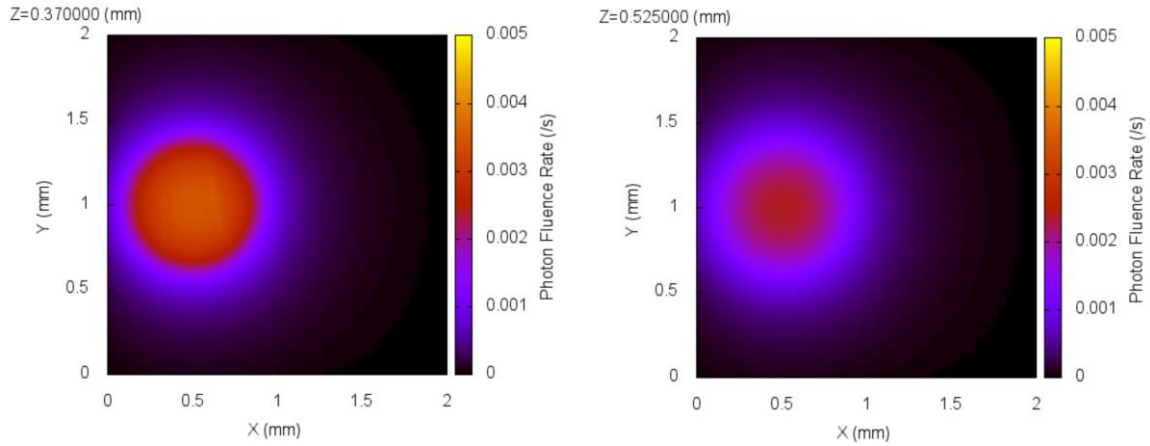


(Fig. 14) Fluence maps deeper within the simulated tissue.

Deeper into the tissue, a second arteriole can be seen very faintly. The laser light becomes more diffuse as absorption has reduced the energy of the beam. The beam is also noticeably wider and less well defined due to the effects of scattering. It is clear from these images that the vast majority of laser light is undetected. It is still unclear where the light that is eventually detected comes from, however. This is where the fluence path analysis can grant insights.

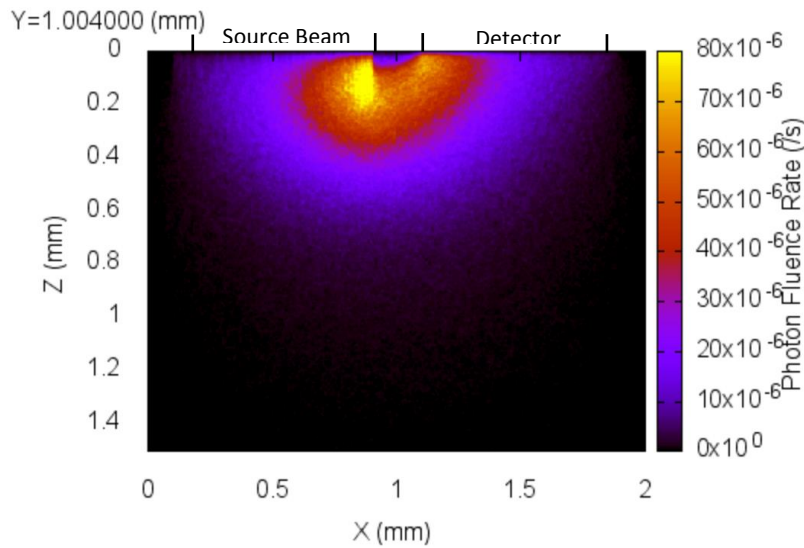


(Fig.15) A fluence map of the detected photons. The slice is made at the centre of the grid and cuts through both the source and the detector.

Fig.15 presents a slice in the Z-X plane of the detected signal. We can see that the majority of the detected signal comes from a region on the near side of the source beam, and this region reaches a depth of approximately 0.2mm. The overall signal zone reaches a depth of approximately 0.6mm, with decreasing sensitivity at greater Z. There are also no noticeable blood vessels in the slice, or indeed any slice along this direction suggesting that this signal shape is not greatly affected by vessel structure.

## DOPPLER SHIFTS

The fluence graphs above indicate the location and relative strength of the detection regions but cannot show where the actual perfusion signal is originating because perfusion relies on frequency shifts. The Doppler maps shown in Fig.16 give a picture of the frequency landscape within the tissue.

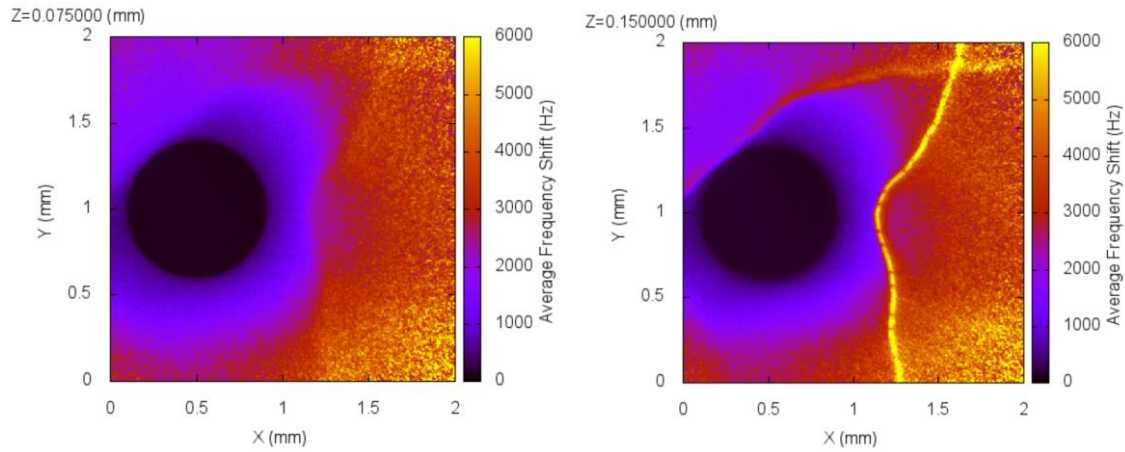


(Fig. 16) The average magnitude of doppler shifts experienced by cells within the tissue simulation, viewed from above at depths of 0.075mm and 0.15mm respectively.

The region of tissue shown in Fig.16 corresponds to the fluence maps seen earlier. There is a distinct dark region in which few frequency shifts have taken place. This shadowed region exists because photons directly along the path of the laser beam have not yet scattered and therefore had no opportunity to acquire a Doppler shift. The Doppler shifts can be seen accumulating further from the beam. The Doppler region on the right hand side has a distorted shape on the surface, and this appears to be due to the blood vessel at 0.15mm depth. The Doppler-inducing blood vessels appear to cast frequency-shifted shadows. The majority of photons in these shadow regions have passed through a blood vessel to enter it, and this suggests that the location of the detector relative to the input beam may have some effect on the measured perfusion. Interestingly, the presence of capillaries can only be seen in dark spots of low frequency shift on the arterioles. This implies the capillaries have a small (and possibly negative) effect on the signal strength. This could be due to the low blood velocity found in the capillaries, which is  $\sim 100$  times less than the velocity in the arterioles. [7]

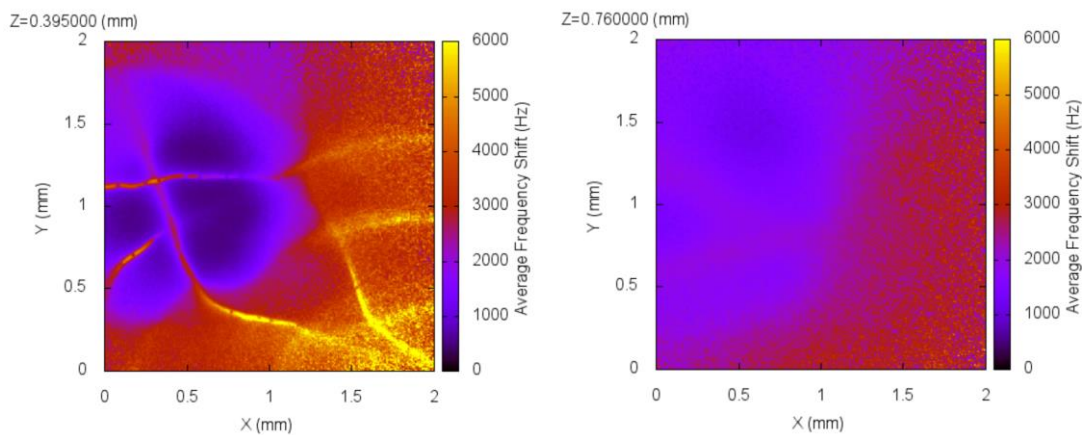


(Fig.17) The average magnitude of Doppler shifts deeper within the tissue.

Fig.17 shows our Doppler signal deeper within the tissue where only a small diffuse portion of the laser light remains un-shifted. There is a strong concentration of blood vessels in the bottom right-hand corner, yielding large Doppler shifts. This same pattern can be seen higher up in the sample, suggesting that the structure deeper within the skin can affect the surface frequencies and hence our perfusion measurement. Below approximately 0.5mm, we are no longer simulating the papillary dermis and so the laser light begins to diffuse towards a homogenous frequency. It was shown earlier that very little of the detected signal comes from this depth, so the behaviour here should be of little consequence.

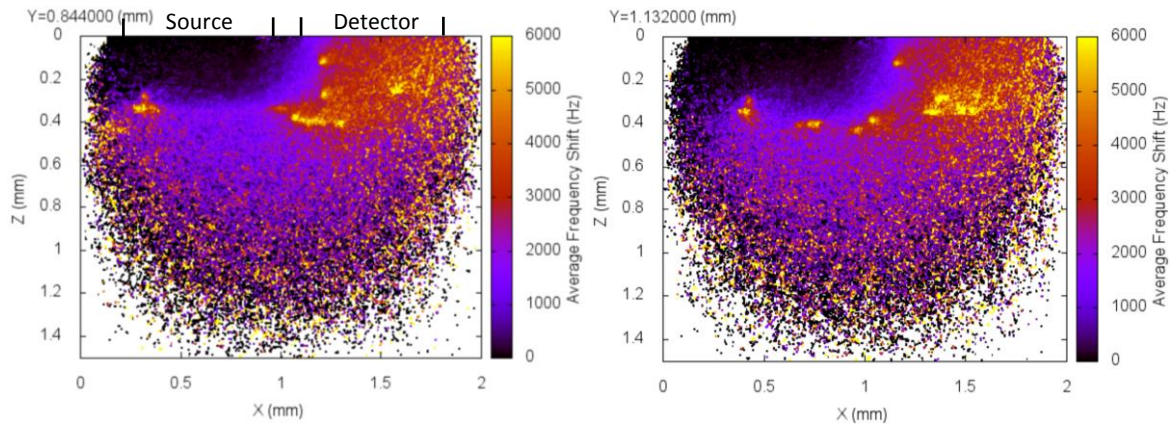


(Fig.18) Slices of the detected Doppler signal in the Z-X plane. The frequency shifts are given as absolute values.

Again, we can isolate the detected photons as shown in Fig.18. The un-shifted input beam can clearly be seen in black. At approximately 0.3mm depth, photons start to encounter blood vessels and the average frequency shift sharply increases to 1000Hz. The arterioles can be easily seen as bright circular structures if moving through the slice or elongated if moving across the slice. The ‘Doppler shadows’ observed in earlier slices can also be seen prominently; each arteriole features a frequency shift trail heading towards the detector (moving with the direction of detected photons). The highly shifted region at large X corresponds to the same region in Fig.17. The vessels visible at 0.4mm depth are responsible for this, confirming earlier suggestions. Additionally, there is another notable absence of capillaries in the image. It seems the vast majority of the perfusion signal in the simulation is coming from the arterioles. As a final note, the grain pattern seen at the side of these images is due to noise. Not enough photons have reached these distant regions to establish a suitable average.

These images offer an insight into the size and magnitude of variations in the Doppler landscape. Outside of the immediate beam vicinity, the surface Doppler shifts can vary by as much as 50% within ~1mm. These surface variations appear to be directly tied to the clustering of vessels deeper within the tissue. Given that the detector has a diameter of 0.8mm, this may explain some of the discrepancies between perfusion values when very close regions of skin are clinically measured.

## THE DETECTED SIGNAL

As shown previously, the detector generates a power spectral density (PSD) that is used to calculate perfusion and CMBC values. These are arbitrarily scaled and therefore only useful when compared to other measurements. The power in using a simulation is that the exact blood velocity and vessel surface area is known. These parameters can be controlled to a level that is not possible with clinical techniques, allowing important relationships between the signal and its source to be explored. In order to firstly validate the blood flow readings, a range of velocities were simulated and plotted alongside their corresponding perfusion value. The blood velocity in a typical arteriole is <20mm/s, so the range used will encompass most clinical measurements. [7]

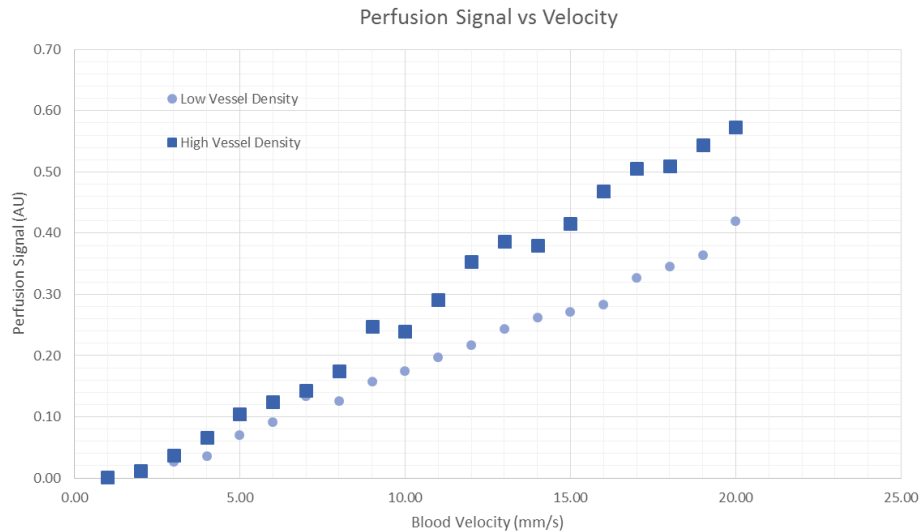


(Fig. 19) The arbitrarily scaled perfusion value is plotted alongside blood velocity. As expected [25], the relationship between perfusion and velocity appears to be linear.

The expected linear relationship between blood velocity and perfusion can be seen in Fig.19. However, it is also clear that blood vessel density has an influence on perfusion sensitivity. We see the measured perfusion value changes with blood velocity at a steeper rate for the higher density sample. In order to quantify this relationship, a range of vessel configurations were generated and each was exposed to a spread of blood velocities.

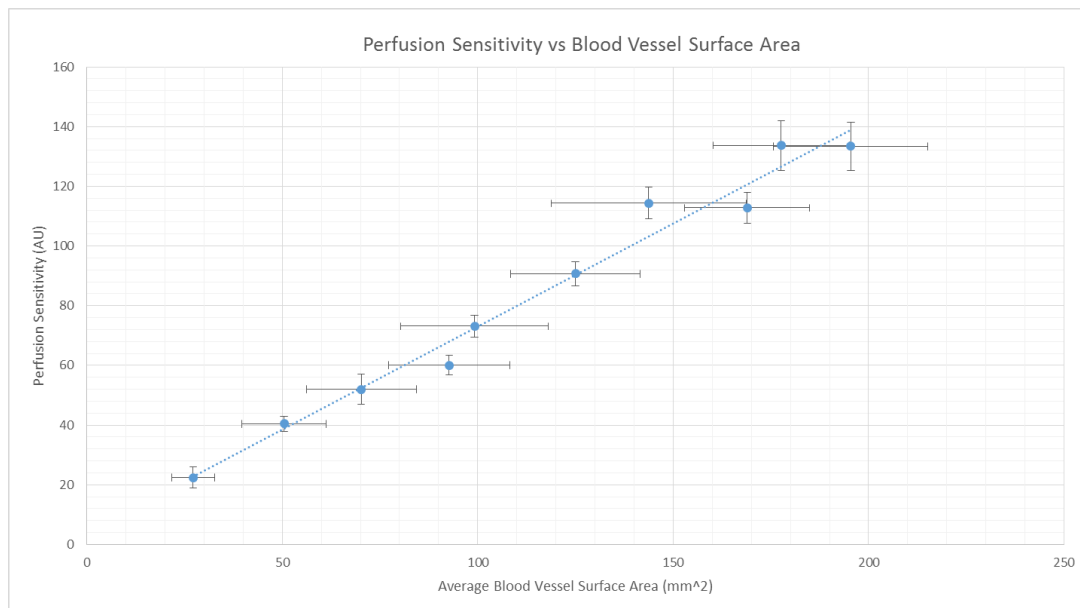


(Fig.20) The gradient of the perfusion/velocity relationship, referred to as 'perfusion sensitivity' is plotted alongside the average blood vessel surface area for different arteriole configurations. There are large uncertainties along the x because of the high degree of variation between successive blood vessel layouts.

We can see from Fig.20 that the relationship between measurement sensitivity and blood vessel surface area appears to be linear. A region with twice the vessel density will be twice as sensitive to perfusion changes.

The relationship shown above has clinical significance. It indicates that changes in perfusion between different individuals cannot be immediately compared. For example, perfusion measurements during clinical research at Ninewells Hospital and Medical School are taken over a period of 25 minutes from the forearm of different volunteers. During this time the flow of blood in the forearm is occluded using an inflated cuff which causes the



measured perfusion value to drop. After a period of time the cuff is released and blood flow returns to normal. An example measurement can be seen in Fig.21. Even if the baseline for every test subject is calibrated to the same level, the measurement changes during occlusion cannot be compared because the magnitude of the perfusion drop is directly related to blood vessel density at each measurement site. We cannot assume this density is similar between different people.

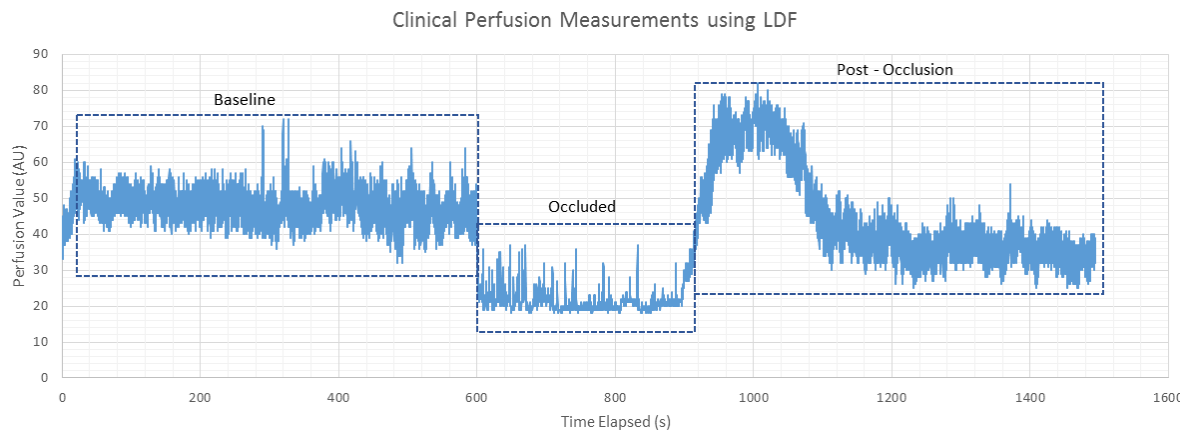


(Fig.21) Clinical perfusion measurements in the forearm over time. The blood flow is occluded after 10 minutes and released after 15 minutes. [28]

If vessel density could be measured, then a correction factor could be applied to make these clinical results more comparable. While this cannot be done easily in practice, there are other results that may be used to indicate vessel density. As explained earlier, the PSD of the detector can also be used to measure the concentration of moving red blood cells (CMBC). The perfusion value was plotted alongside this CMBC to assess its use as a calibration constant.

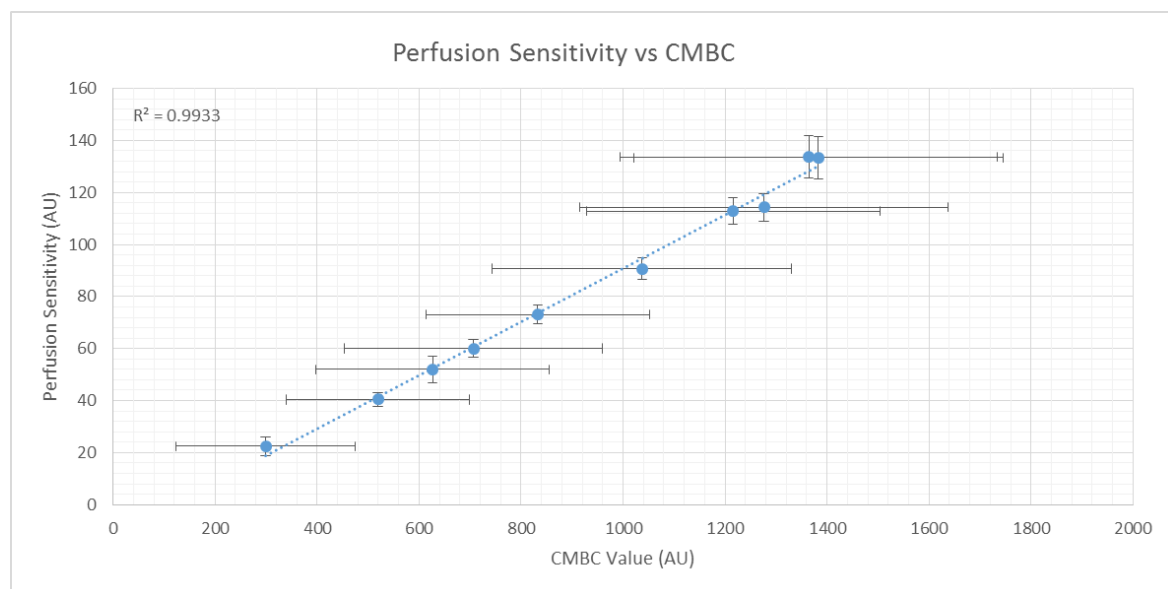


Fig.22 Detected perfusion value was plotted alongside CMBC for the same collection of vessel configurations shown in Fig. 20

We see that perfusion scales approximately linearly with CMBC in Fig.22. There is an even larger degree of variation in the x-axis however. The spread of possible CMBC's for a particular vessel surface area is compounded by the pre-existing spread in vessel surface areas for each data point.

The effects of vessel count and blood velocity on CMBC

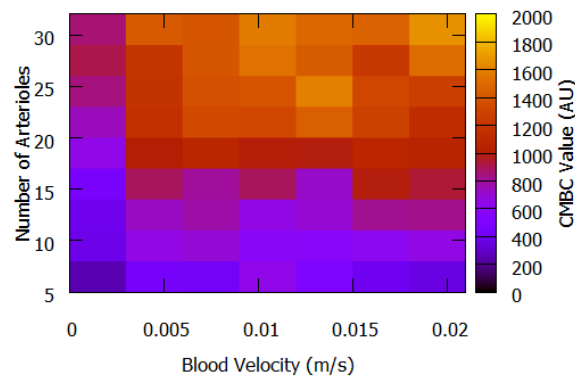
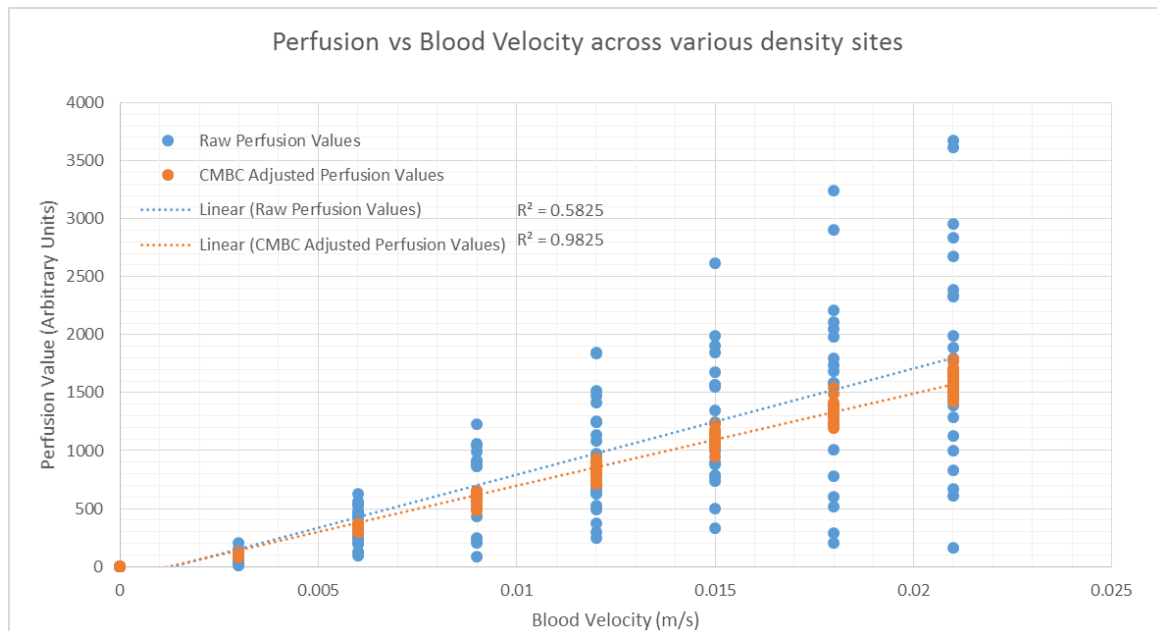


Fig.23 A heat map to show the influence of blood velocity on CMBC across numerous blood vessel sites.

CMBC is only useful as a correction coefficient if it is independent of blood flow because it will otherwise have a dependence on perfusion value. This relationship is tested in Fig.23. We see a general trend of increasing CMBC with greater Arteriole count as expected. The dependence on blood velocity does not appear to follow a general trend besides some degree of noise. The notable exception is at zero blood velocity. This is beyond the bounds of our PSD relation on which our CMBC calculation depends, and so any CMBC values here are expected to be anomalous. The true concentration of moving blood cells is zero under these conditions. From this data, it seems that CMBC has very little dependence on blood velocity up to 0.02m/s. As a proof-of-concept, we can use this CMBC to standardise the perfusion measurements across many different sites, shown in Fig.24. There is a substantial increase in concordance between the perfusion data and the linear trend-line when vessel density is accounted for in this way. The R-squared value rises from 0.5825 to 0.9825. It appears that the CMBC can be an effective tool for standardising perfusion measurements if we assume that perfusion differences between sites are due exclusively to blood vessel velocity and density differences. As the LDF signal is by nature only sensitive to moving components such as these, this is a very significant result.



(Fig.24) The perfusion-velocity relationship is displayed for various blood vessel configurations and densities. An 'adjusted' perfusion value is generated by dividing the raw perfusion value by the CMBC, and then multiplying by the average CMBC to bring it onto a comparable scale.

While CMBC information can quite easily be obtained from the same detector that yields perfusion measurements as demonstrated, not all research devices make this information available. The LAKK-M device on which the simulation was based is one example. In order to allow collaborators at Ninewells Hospital and Medical School to standardise perfusion values, an alternative method was found in the use of 'blood volumes'. A blood volume measurement describes the proportion of laser light absorbed by haemoglobin compared to the rest of the tissue and is measured using a separate detector. [5] This was calculated in the simulation by simply counting photons absorbed in the blood vs photons absorbed in total. The results seen in Fig.25 show that blood volume is a potential, albeit less effective alternative to CMBC. It was found to be particularly erroneous at low vessel densities where some extreme outliers 2-3 times greater than any other value had to be excluded. Nonetheless, there was an increase in linear concordance to 0.8681 when a blood-volume based adjustment was applied. The high variance in blood volume results could be due to the relatively small number of sample photons applied to the tissue. Performing a large number of simulations like this is computationally expensive, and so the photon count was limited to ~1 million. For the CMBC graph this is less of a problem because a photon only needs to be detected to contribute to the PSD. For blood volume calculation however, photons need to be absorbed. Due to tissue transparency in the 1064nm regime, the total number of photons absorbed by the blood numbered in the thousands, which a comparably small sample.

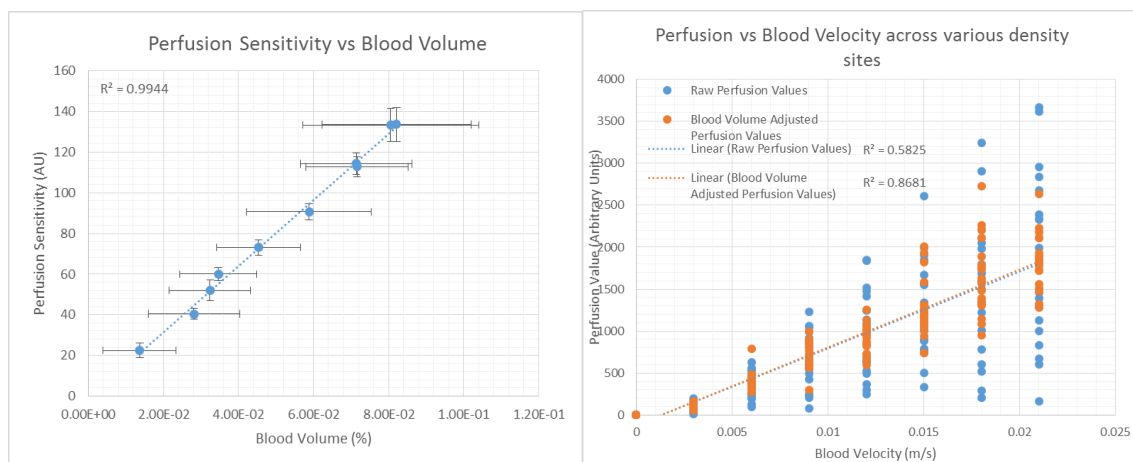


(Fig.25) Perfusion sensitivity is correlated to blood volume in a similar way to CMBC. It can also be used to standardise perfusion values, albeit less effectively.

## FURTHER DEVELOPMENT

The simulation described in this report can be used as a foundation for future models. Some interesting relationships and behaviours have been observed that warrant further investigation and clinical validation. Additionally, there are some areas that could be improved to make conclusions drawn from the model more robust.

The relationship obtained between perfusion sensitivity and vessel density is highly significant if it can be clinically reproduced. This may require modification to the MLNDS software such that the PSD of the photodetector is accessible for CMBC calculation. Alternatively, the blood volume value demonstrated earlier could be investigated. As explained, the high blood volume variance may partly be due to the limited number of photons being applied. This hypothesis could be easily tested by running the simulation on more powerful computer hardware than was available for the duration of this project. If the CMBC relationship cannot be reproduced clinically then the vessel model may need upgrading. In this scenario the assumption that blood vessels are the only significant source of Doppler shifts could be false. Alternatively, the vessel structure may need refining. The parabolic shapes held by capillaries were found to be unrealistic. The results suggest that they have a relatively small contribution to the Doppler signal, but this may have been biased by their shape. It may be beneficial to abandon the parabola entirely and assume a random-walk similar to the arteriole method.



Ultimately however, the arrangement of blood vessels in live tissue is not *completely* random. The microcirculation is arranged such that all respiring cells in the body have access to the blood supply. A future tissue model may need to be aware of this, filling in voids when necessary and avoiding inefficient overlaps between vessels.

A separate and unexplored component of the microcirculation was its time evolution. Much of the clinical research with LDF concerns the time response of perfusion to external stimuli. This can include the analysis of important oscillations in the blood flow [29]. The blood supply is not static however, and so any time dependence in the blood velocity may also require a time dependence in the vessel structure. This could present a very challenging simulation problem.

## CONCLUSIONS

Although the basic technology has existed for over two decades, medical laser Doppler techniques remain an area of active research and development. These promising methods could one day be used to diagnose diabetes and cardiovascular diseases both quickly and non-invasively. However, the current lack of standardisation across measurements will need to be overcome before this can be achieved [30]. The work presented in this report is another step toward this goal. It has been shown that the LDF technique can be simulated with the Monte Carlo method using a tissue model of discrete blood vessels. By studying the Doppler shifts induced by these vessels across the tissue, regions of high and low signal level have been identified and attributed to the clustering of blood vessels below the skin. Such behaviour may explain the high degree of spatial variation experienced by LDF probes. The signal received by the detector was then isolated and visualised and can be seen taking a curved path between the source and detector that is similar to previous findings [9]. The majority of this Doppler signal was found to originate from arterioles crossing between the beam and the detector. After running the simulation in numerous configurations, a positive linear relationship between perfusion sensitivity and vessel density emerged; regions with twice the blood vessel density had a perfusion value twice as sensitive to changes in blood flow. This result further implies that vessel density contributes to the LDF measurement discrepancies across different skin sites. A method for correcting this was obtained in which perfusion values were weighted by their corresponding CMBC values. This technique proved very effective in the model case but still needs to be verified clinically. In the future, if the standardisation technique described here or in similar works can be clinically reproduced, they could help pave the way for clinical diagnosis with laser Doppler techniques.

## BIBLIOGRAPHY

- [1] R. Eckhardt, "Stan Ulam, John von Neumann and the Monte Carlo Method," *Los Alamos Science*, vol. 15, 1987.
- [2] M. Roustit and J.-L. Cracowski, "Assessment of endothelial and neurovascular function in human skin microcirculation," *Trends in Pharmacological Sciences*, vol. 34, no. 7, p. 375, 2013.
- [3] D. J. Gawkrödger, "Microanatomy of the Skin," in *Dermatology: An Illustrated Colour Text*, Elsevier, 2008, pp. 2-3.
- [4] M. Roustit and J.-L. Cracowski, "Assessment of endothelial and neurovascular function in human skin microcirculation," *Trends in Pharmacological Sciences*, vol. 34, no. 7, pp. 373-374, 2013.
- [5] E. U. Rafailov, K. S. Litvinova and S. G. Sokolovski, "Towards novel compact laser sources for non-invasive diagnostics and treatment," in *Proc. SPIE 9550, Biosensing and Nanomedicine VIII*, 2015.
- [6] A. Csillag, "Chapter 5: The Skin," in *Atlas of The Sensory Organs*, Humana Press, 2005, pp. 207-213.
- [7] A. C. Guyton and J. E. Hall, "Overview of the Circulation; Biophysics of Pressure, Flow and Resistance," in *Guyton and Hall Textbook of Medical Physiology Twelfth Edition*, Elsevier, 2011, p. 25.
- [8] M. Johannes Koehler, T. Vogel, P. Elsner, K. König, R. Buckle and M. Kaatz, "In vivo measurement of the human epidermal thickness in different localizations by multiphoton laser tomography," *Skin Research and Technology*, vol. 16, pp. 259-264, 2010.
- [9] I. Fredriksson, M. Larsson and T. Strömberg, "Measurement depth and volume in laser Doppler flowmetry," *Microvascular Research*, vol. 78, pp. 4-13, 2009.
- [10] I. Fredriksson, M. Larsson and T. Strömberg, "Optical microcirculatory skin model: assessed by Monte Carlo simulations paired with in vivo laser Doppler flowmetry," *Journal of Biomedical Optics*, vol. 13, p. 014015, 2008.
- [11] S. L. Jacques, "Optical properties of biological tissues: a review," *Physics in Medicine and Biology*, vol. 58, pp. R54-R58, 2013.
- [12] S. L. Jacques, "Optical properties of biological tissues: a review," *Physics in Medicine and Biology*, vol. 58, pp. R51-R53, 2013.
- [13] "Tissue Spectra," UCL Biomedical Optics Research Laboratory, [Online]. Available: <http://www.ucl.ac.uk/medphys/research/borl/intro/spectra>. [Accessed 28 March 2016].

- [14] L. Kou, D. Labrie and P. Chylek, "Refractive indices of water and ice in the 0.65-2.5 micrometer spectral range," *Applied Optics*, vol. 32, pp. 3531-3540, 1993.
- [15] S. L. Jacques, "Optical properties of biological tissues: a review," *Physics in Medicine and Biology*, vol. 58, p. R50, 2013.
- [16] T. L. Troy and S. N. Thennadil, "Optical properties of human skin in the near infrared wavelength range of 1000 to 2200 nm," *Journal of Biomedical Optics*, vol. 6, no. 2, pp. 167-176, 2001.
- [17] S. L. Jacques, "Optical properties of biological tissues: a review," *Physics in Medicine and Biology*, vol. 58, pp. R39-R48, 2013.
- [18] E. Salomatina, B. Jiang, J. Novak and A. N. Yaroslavsky, "Optical properties of normal and cancerous human skin in the visible and near-infrared spectral range," *Journal of Biomedical Optics*, vol. 11, no. 6, 2006.
- [19] I. M. Braverman, A. Keh and D. Goldminz, "Correlation of Laser Doppler Wave Patterns with Underlying Microvascular Anatomy," *The Journal of Investigative Dermatology*, vol. 95, no. 3, pp. 383-386, 1990.
- [20] K. Wood, B. Whitney, J. Bjorkman and M. Wolff, *Introduction to Monte Carlo Radiation Transfer*, 2013.
- [21] L. G. Henyey and J. L. Greenstein, "Diffuse radiation in the Galaxy," *Astrophysical Journal*, vol. 93, pp. 70-83, 1941.
- [22] A. N. Witt, "Multiple Scattering in Reflection Nebulae I. A Monte Carlo Approach," *Astrophysical Journal Supplement Series*, vol. 35, pp. 1-6, 1977.
- [23] S. L. Jacques and S. A. Prahl, "Henyey-Greenstein scattering function," Oregon Medical Laser Center, 1998. [Online]. Available: <http://omlc.org/education/ece532/class3/hg.html>. [Accessed 24 April 2016].
- [24] S. L. Jacques, "Chapter 5: Monte Carlo Modeling of Light Transport in Tissue," in *In Optical-Thermal Responses of Laser-Irradiated Tissue, 2nd Edition*, Springer, 2009, pp. 19-21.
- [25] I. Fredriksson, C. Fors and J. Johansson, "Laser Doppler Flowmetry - a Theoretical Framework," Department of Biomedical Engineering, Linköping University, 2007.
- [26] L. B. Lucy, "Improved Monte Carlo techniques for the spectral synthesis of supernovae," *Astronomy and Astrophysics*, vol. 345, pp. 221-220, 1999.
- [27] M. H. Koelink, F. F. M. de Mul, J. Greve, R. Graaff, A. C. M. Dassel and J. G. Aarnoudse, "Monte Carlo simulations and measurements of signals in laser Doppler flowmetry on human skin," in *SPIE Proceedings Vol. 1431: Time-Resolved Spectroscopy and Imaging of Tissues*, 63, 1991.
- [28] S. Smirni, *Original LDF Measurements*, Dundee: Ninewells Hospital and Medical School, 2016.

- [29] G. E. C. Nogueira and M. S. Folgosi-Correa, "Quantifying low-frequency fluctuations in the laser Doppler flow signal from human skin," in *SPIE Proceedings Vol. 7898: Dynamics and Fluctuations in Biomedical Photonics VIII*, 2011.
- [30] M. Roustit and J.-I. Cracowski, "Non-invasive Assessment of Skin Microvascular Function in Humans: An Insight Into Methods," *Microcirculation*, vol. 19, pp. 47-59, 2011.